coatings

MDPI

Article

The Effect of Precipitates on the Stress Rupture Properties of Laser Powder Bed Fusion Inconel 718 Alloy

Jinhong Du [1], Wenhao Cheng [1,2], Yiming Sun [2], Rui Ma [3], Hongbing Liu [1,*], Xiaoguo Song [2,*], Jin Yang [1] and Caiwang Tan [2]

[1] School of Materials Engineering, Shanghai University of Engineering Science, Shanghai 210620, China; dujinhong2022@163.com (J.D.)
[2] State Key Laboratory of Advanced Welding and Joining, Harbin Institute of Technology, Harbin 150001, China
[3] Beijing Power Machinery Institute, Beijing 100074, China
* Correspondence: lhongbing@163.com (H.L.); songxg@hitwh.edu.cn (X.S.)

Abstract: Improving the high-temperature stress rupture properties of Inconel 718 (IN718) alloys is crucial for enhancing aircraft engine performance. By using the laser powder bed fusion (LPBF) technique, IN718 alloys were crafted at varying volumetric energy densities (VED) in this study. The dendrite growth mode, reinforcing phase distribution and high temperature stress rupture properties of various VED samples were investigated. The results showed that the stress rupture life and the uniform elongation of the samples both first increased and then decreased with the increase in VED. When the VED was 60 J/mm^3, the maximum rupture life and elongation of the sample were 43 h and 3.8%, respectively. As the VED increased, the angle of dislocation in the dendrite decreased while the spacing between primary dendrite arms increased, resulting in an increase in the size and volume fraction of the Laves phase. Following a heat treatment, the δ phase would nucleate preferentially around the dissolved Laves phase causing an increase in the volume fraction of the δ phase with the increase in VED. The creep voids readily formed around the δ phase are distributed along the grain boundaries, while the inhomogeneous δ phase and fine grains facilitated crack initiation and propagation. Furthermore, a significant quantity of the δ phase consumed the Nb element, thereby hindering adequate precipitation in the γ″ phase and causing cracks.

Keywords: volume energy density; laser powder bed fusion; Inconel 718 alloy; precipitates; stress rupture properties

Citation: Du, J.; Cheng, W.; Sun, Y.; Ma, R.; Liu, H.; Song, X.; Yang, J.; Tan, C. The Effect of Precipitates on the Stress Rupture Properties of Laser Powder Bed Fusion Inconel 718 Alloy. *Coatings* **2023**, *13*, 2087. https://doi.org/10.3390/coatings13122087

Academic Editor: Hideyuki Murakami

Received: 24 November 2023
Revised: 10 December 2023
Accepted: 13 December 2023
Published: 14 December 2023

1. Introduction

Nickel-based superalloys are gaining popularity owing to their exceptional mechanical properties at high temperatures [1]. Inconel 718 (IN718) is a nickel-based superalloy which finds extensive application in the aviation, aerospace, chemical and energy sectors [2,3]. The alloy exhibits exceptional mechanical properties up to 650 °C, making it well-suited for producing sophisticated components with a high worth and effectiveness, including combustion chamber casings, compressor disks, and turbines [4–6]. Incorporating structural and functional elements into complex components is becoming a crucial means of enhancing performance and innovation for aero-engines and gas turbines [7,8]. However, traditional material processing cannot meet the requirements of integrating lightweight and complex components. Thus, there is a pressing need for a technology that can successfully fulfil the geometric and mechanical requirements of the products.

The integration of structural and functional properties into complex components has gradually become an important approach for innovating and enhancing the performance of aero-engines and gas turbines. However, traditional material processing cannot meet the requirements of integrating lightweight and complex components. Thus, it is imperative to develop a technology that can fulfil the geometric and mechanical specifications of products.

Laser powder bed fusion (LPBF) was developed from the basic principle of prototype manufacturing technology. A three-dimensional digital model of the part was sliced and layered with special software, and the high-energy laser beam was used to selectively melt the metal powder to manufacture 3D solid parts [9–11]. LPBF becomes a key candidate for manufacturing complex IN718 alloy parts due to its cost-effective and time-saving processing features [12].

Many authors have studied the effects of process parameters on the mechanical properties of LPBF IN718 [13–15]. Yang et al. [16] observed that an extension of laser energy resulted in a decrease in tensile power due to the enlargement of the Laves phase. Du et al. [17] studied the effects of build direction on the microstructure and tensile sections of LPBF IN718. It was once found that the fraction of Laves segment and the strength of samples extended with a growing incline angle in the construct direction. The process parameters affected the microstructure and mechanical properties of LPBF IN718 alloy mainly by controlling the Laves phase. However, the Laves phase would be converted to the δ phase after heat treatment, and the δ phase has a greater impact on the high-temperature mechanical properties of the material [18–20].

The presence of the δ phase has been shown, in multiple studies, to alter the microstructure and enhance the mechanical properties of the LPBF IN718 alloy. Zhang et al. [21] studied its high-temperature stress rupture properties and found that samples without an δ phase at grain boundaries had the best stress rupture properties. Shi et al. [22] demonstrated that the heat-treated samples were prone to forming creep voids and microcracks around the δ phase at the grain boundaries during the creep rupture test, thereby accelerating the occurrence of fracture behavior. Gao et al. [20] discovered that an appropriate heat treatment can regulate the morphology and distribution of the δ-phase, leading to an enhancement in the high-temperature mechanical properties of the IN718 alloy. Nonetheless, the latest research has solely examined the impact of different heat treatment methods on the δ phase and mechanical characteristics. The effect of different VEDs on the precipitation behavior in the Laves phase, and the effect of the Laves phase in the as-deposited sample on volume fraction and the distribution of the δ phase after heat treatment deserve further investigation.

The study aims to examine how the Laves phase affects precipitation in the δ phase in samples with varying VED and its impact on stress rupture properties. Additionally, the research aims to establish the relationship between process parameters, precipitates and high-temperature mechanical properties.

2. Materials and Methods

The experiment was conducted using an EOS M290 machine which was fitted with a Yb-fiber laser with a maximum capacity of 400 W. The stainless substrate underwent preheating to reach a temperature of 80 °C. During the printing process, the oxygen content was kept below 100 ppm, and argon was utilized as a protective gas. The chemical composition of the gas atomized IN718 powder is shown in Table 1. The particle size of the IN718 powder ranged from 15 μm to 53 μm, and the scanning electron microscope (SEM) images of the powder are shown in Figure 1. The main parameters are shown in Table 2. The formula for calculating the VED is shown in Equation (1):

$$VED = \frac{P}{v \cdot h \cdot t} \quad (1)$$

where P is the power of the laser, v is the scanning speed, h is the distance between the hatches and t is the thickness of the layer. The scanning strategy was striped, and the layers were rotated by 67°. The as-deposited samples with different *VED* were named S1, S2 and S3, respectively. The as-deposited samples were heat treated in accordance with the industry standard heat treatment for wrought IN718 alloy [23].

Table 1. The chemical composition of IN718 powder.

Element	Ni	Cr	Nb	Mo	Al	Mn	Si	C	S	Fe
Wt%	52.53	20.19	4.85	3.10	0.5	0.055	0.041	0.025	0.001	Bal.

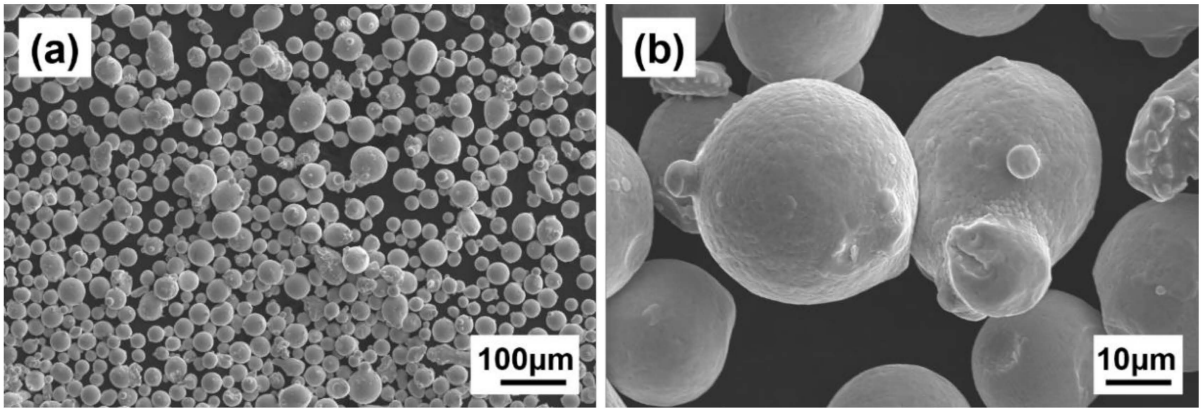

Figure 1. SEM images characterizing particle size in IN718 powder: (**a**) 1000×, (**b**) 5000×.

Table 2. The parameters of the LPBF process.

Designation	Laser Power (W)	Scanning Velocity (mm/s)	Hatch (mm)	Thickness (mm)	Volume Energy Density (J/mm^3)
S1	210	1000	0.1	0.04	52.5
S2	240				60
S3	300				75

The specific heat treatment was as follows: solution heat treated at 980 °C for 1 h followed by compressed argon cooling to room temperature and 2-stage ageing: 720 °C for 8 h followed by furnace cooling to 620 °C at a cooling rate of 50 °C/h; then the samples were held at 620 °C for 8 h before air cooling to room temperature. After heat treatment, the samples were designated as H-S1, H-S2 and H-S3, respectively.

The metallographic samples prepared by LPBF were initially ground and subsequently polished. When grinding, sandpaper is used in this order (120 mesh, 400 mesh, 800 mesh, 1200 mesh, 2000 mesh, 2500 mesh). After we finished polishing, polishing pastes of W5, W2.5 and W.5 were used for polishing. Afterwards, the polished samples were subjected to etching in a solution containing (5 g $CuCl_2$ + 7 g $FeCl_3$ + 100 mL HCl + 20 mL HNO_3 + 100 of H_2O) for a duration of 20 s. Microstructure investigations were conducted utilizing an optical microscope (OM) and SEM equipment. The Tecnai G2 F30 S-TWIN (FEI Nano Ports Co., Ltd., Waltham, MA, USA) transmission electron microscope (TEM) was employed to identify the distribution of the strengthening phases. TEM samples were prepared using the focused ion beam (FIB) method, and the thickness of the samples was about 100 nm. The Image J software (v1.53) was used to measure strengthening phases size.

Rupture tests were conducted to evaluate the high-temperature mechanical properties of the IN718 alloy. Test samples for the rupture tests were prepared following the ASTM E139 standard [24], as shown in Figure 2. The rupture test was conducted at a temperature of 650 °C and a pressure of 690 MPa on a rupture testing machine RDL100 (Jiangsu Wallong-Hsin Machinery Engineering Corporation Co., Ltd., Wuxi, China). Three samples were tested in each set of experiments.

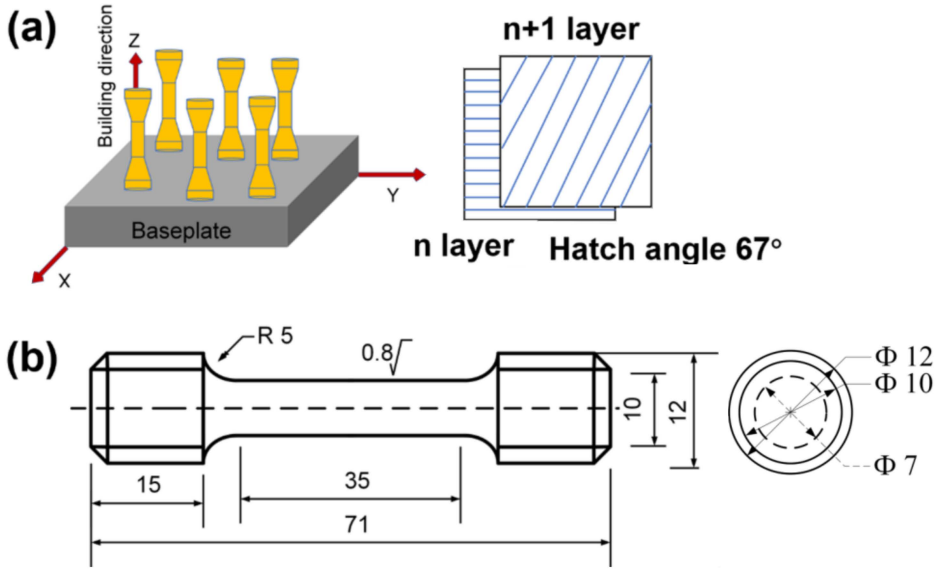

Figure 2. (**a**) Samples of LPBF process, (**b**) Dimensions of stress rupture samples (unit: mm).

3. Results and Discussion

3.1. Microstructure Evolution of LPBF IN718

The microstructure of the as-deposited sample, in the direction of building, is provided in Figure 3. The microstructure of all samples exhibited a characteristic fish-scale appearance along the *X*-*Z* direction, which is represented in Figure 3a–c. The columnar grains grew mainly due to the heat flow direction during the solidification of the molten pool being nearly parallel to the deposition direction, and the competitive growth of grains [25]. In as-deposited LPBF IN718 alloy samples, the depth and width of the molten pool increased with greater VED. The length and width of the molten pool were greater for high power laser samples than for low power ones. A higher laser power resulted in grains that were prone to epitaxial growth. Overlapping areas could re-melt and re-solidify during the melting of adjacent tracks or layers due to the high laser power [16,26].

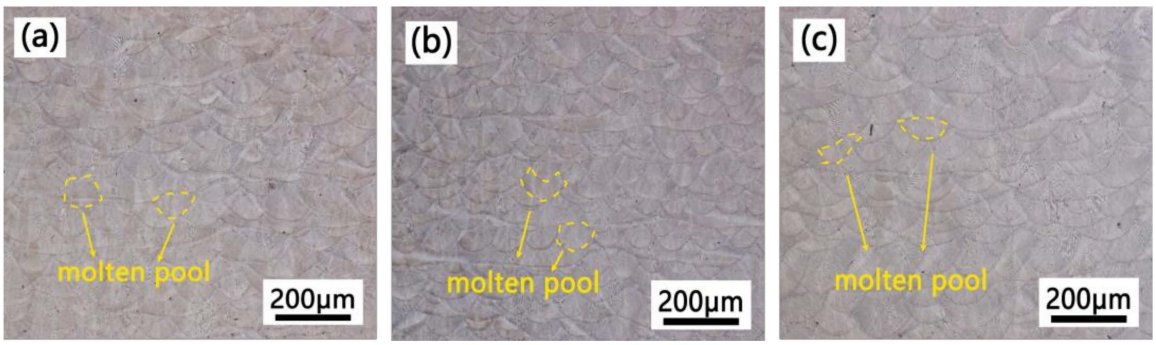

Figure 3. OM images on build direction of the as-deposited IN718 samples: (**a**) S1, (**b**) S2, (**c**) S3.

The segregation of elements (Nb, Mo, Ti) in IN718 alloy leads to the formation of a large number of Laves phases between the molten layers of the alloy [7,27]. The interdendritic region was particularly susceptible to the formation of the Laves phase, as shown in Figure 4a–c. The Laves phase typically measured 1–2 μm in length, and its chemical formula was (Ni, Fe, Cr)2(Nb, Mo, Ti) [28]. The Laves phase would dissolve and transform into the δ phase after heat treatment. The microstructures of the samples post heat treatment are presented in Figure 4d–f. The δ phase was visible in both needle-like and short rod-like shapes. Moreover, the δ phase generally had a size of 0.5–1 μm and a chemical formula of Ni_3Nb in the IN718 alloy [29]. Using Image J software (v1.53), the volume fraction of the Laves and δ phase was determined through statistical analysis (Figure 5). The volume

fractions of the Laves phase in different VED samples were calculated to be 6.35%, 7.75% and 9.86%, respectively. After undergoing heat treatment, the respective volume fractions in the δ phase in the three samples were 4.74%, 5.54%, and 7.83%, respectively. The volume fractions of both Laves and δ phases increased with an increase in VED.

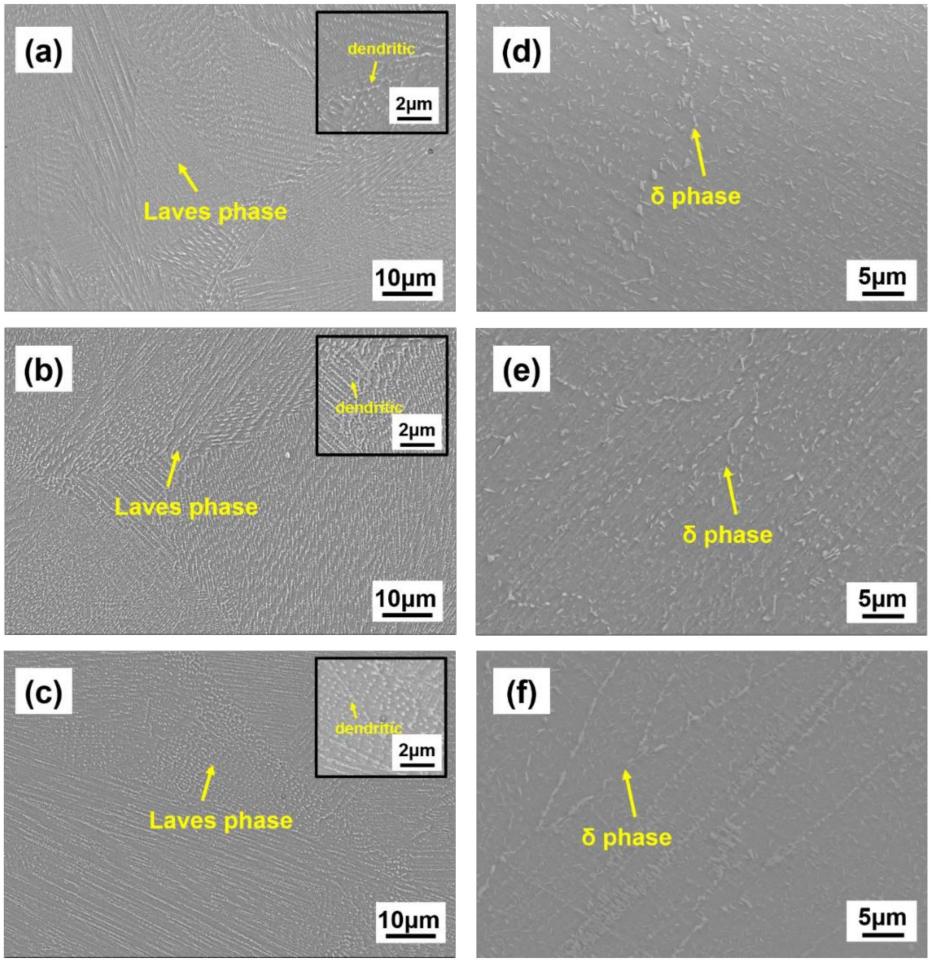

Figure 4. SEM images on build direction of the as-deposited and heat-treated IN718 samples: (**a**) S1, (**b**) S2, (**c**) S3, (**d**) H-S1, (**e**) H-S2, (**f**) H-S3.

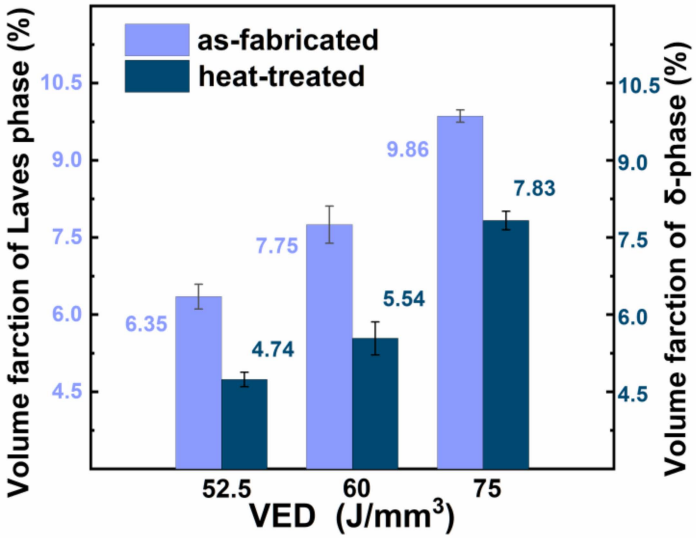

Figure 5. The volume fraction of Laves phase and δ phase in diverse VED samples.

To compare element distribution and precipitate morphologies in the as-deposited and heat-treated samples, we selected S2 and H-S2 for TEM observation. High-angle annular dark field (HAADF) TEM micrographs for the Laves and δ phases appear in Figure 6a,c, respectively. High-density entangled dislocations were found in the intergranular boundaries and matrix regions of S2, in addition to precipitates. The distribution of the main elements can be observed in Figure 6b,d using X-ray energy dispersive spectroscope (XEDS) elemental mapping from the white dotted square. Continual segregation of Nb, Mo and Ti and numerous precipitates along the cellular boundary were observed in the as-deposited sample. However, in H-S2, partial dissolution of the Nb, Mo, and Ti segregation occurred after solution treatment, and the γ'/γ'' phases were precipitated during the aging stage. The entangled dislocations of high density vanished, resulting in a more uniform microstructure.

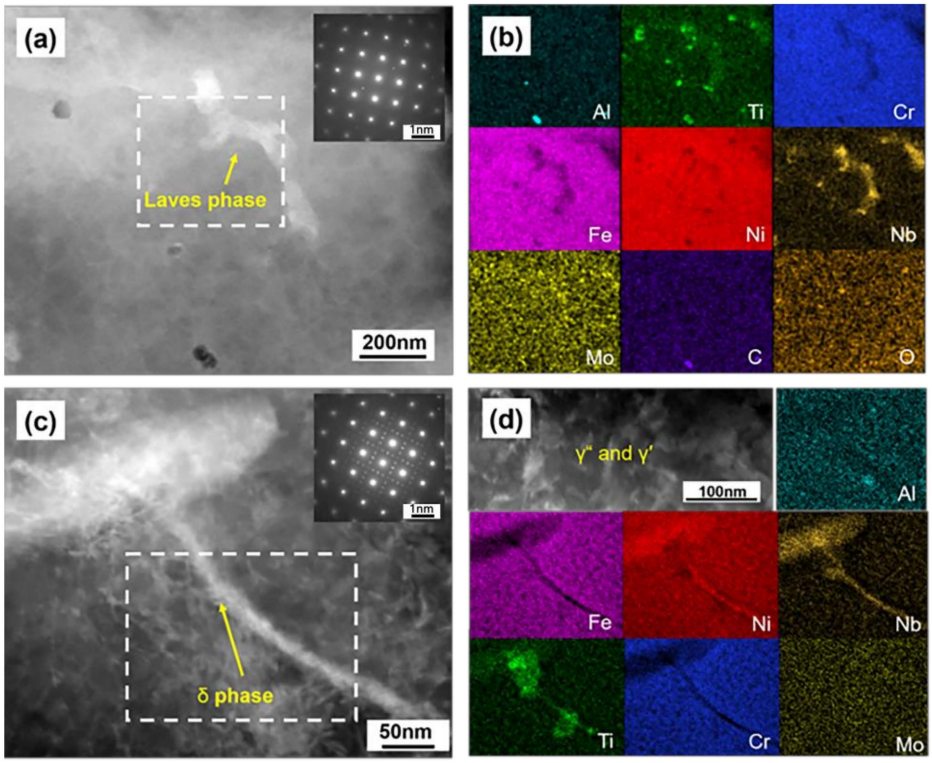

Figure 6. HAADF STEM micrographs and XEDS elemental mapping from the white square: (**a**,**b**) as-deposited sample, (**c**,**d**) heat-treated sample.

3.2. Stress Rupture Properties of LPBF IN718

The stress rupture characteristics of the three sample groups following heat treatment at high temperatures are depicted in Figure 7. The average rupture life of the three samples were 19.5 h, 43.0 h and 32.1 h, respectively. The three samples displayed similar, unsatisfactory elongation rates of only 2.3%, 3.8% and 2.8%, respectively. The average rupture life and elongation of the three samples initially rose before decreasing alongside the increment of VED.

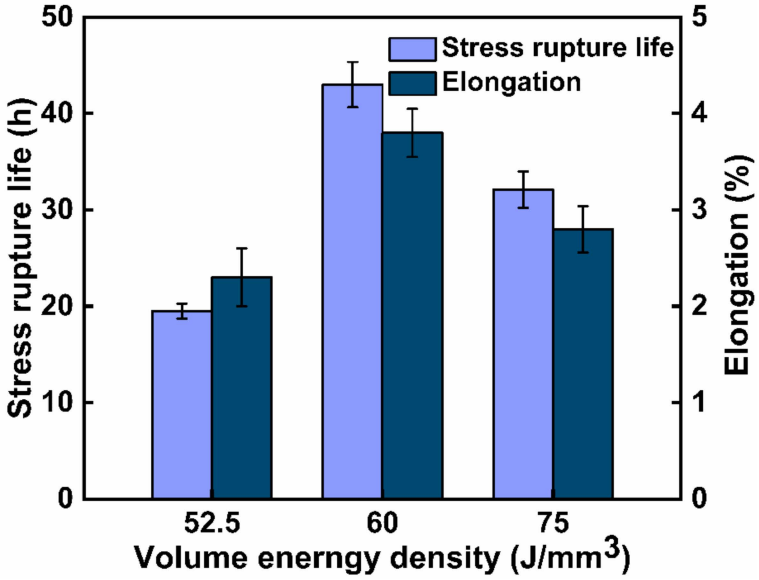

Figure 7. Stress rupture properties of IN 718 at different VEDs.

The fracture surfaces of three samples, as depicted in Figure 8, exhibited intergranular fracture. The mode of fracture was primarily brittle, and the fracture surface was plain, with small and shallow dimples observed in all three samples. As a result, the elongation of the three samples was limited. Micro-voids developed at the interface between the strengthening phase particles and the matrix, facilitating the generation of dimples.

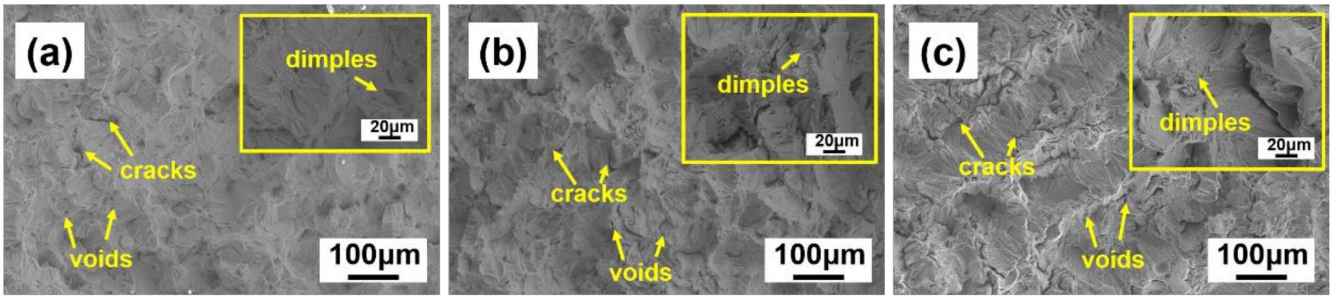

Figure 8. Fractured surface of the samples after creep: (**a**) H-S1, (**b**) H-S2, (**c**) H-S3.

3.3. Analysis of Precipitates in Samples with Different VEDs

To better depict the progression of the Laves phases in the three sample types, the Image J software (v1.53) was employed to tally the lengths, widths and aspect ratios of the Laves phases. Figure 9 demonstrated the statistical findings, whereby the size of the Laves phase grew with increasing VED. The length increased at a slower rate than the average width of the Laves phase, resulting in the aspect ratio of the Laves phase being the smallest in S3 (Figure 9d). The formation of the Laves phase occurred within the interdendritic region during solidification. The morphologies and distributions of the phase were determined primarily by the behavior of dendrite growth [30]. The conventional model for columnar dendrite grain growth suggests that dendrite orientation primarily depends on undercooling differences [31]. For the IN718 alloy, this direction was along its <001> crystallographic orientation, which formed the smallest angle with the local temperature gradient. Each dendrite arm had a misalignment angle θ relative to the temperature gradient ($-45^\circ \leq \theta \leq 45^\circ$ for the 2-D case), as presented in Figure 10a. The V_θ denoted the growth rate of the dendrite arm and was calculated by dividing VL (the velocity of the liquidus isotherm) by the cosine of θ. The cooling rate of molten materials was negatively correlated with the VED, thus a decreasing trend for the misalignment angle

θ was shown in S1–S3. In addition, Equation (2) [32] was commonly used to determine the primary dendrite arm spacing (*PDAS*, measured in mm).

$$PDAS = 80\varepsilon^{-0.33} \quad (2)$$

where *PDAS* is the primary dendrite arm spacing of laves phase. ε is cooling rate of molten pool. From the formula, it can be found that *PDAS* was inversely proportional to the cooling rate (ε, K/s). As the VED increased, the samples exhibited a larger PDAS and a smaller misalignment angle θ, as shown in Figure 10b. A small *PDAS* and a large misalignment angle θ easily caused a dense distribution in the Laves phase, as shown in Figure 10c. In contrast, the slower cooling rate at a high VED allowed enough time for Nb, Mo and Ti atoms to diffuse into the interdimer region. This led to the enrichment of abundant atomic groups which served as nucleation sites for the Laves phase. Therefore, more Laves phases were formed at higher VED samples, as shown in Figures 5 and 9.

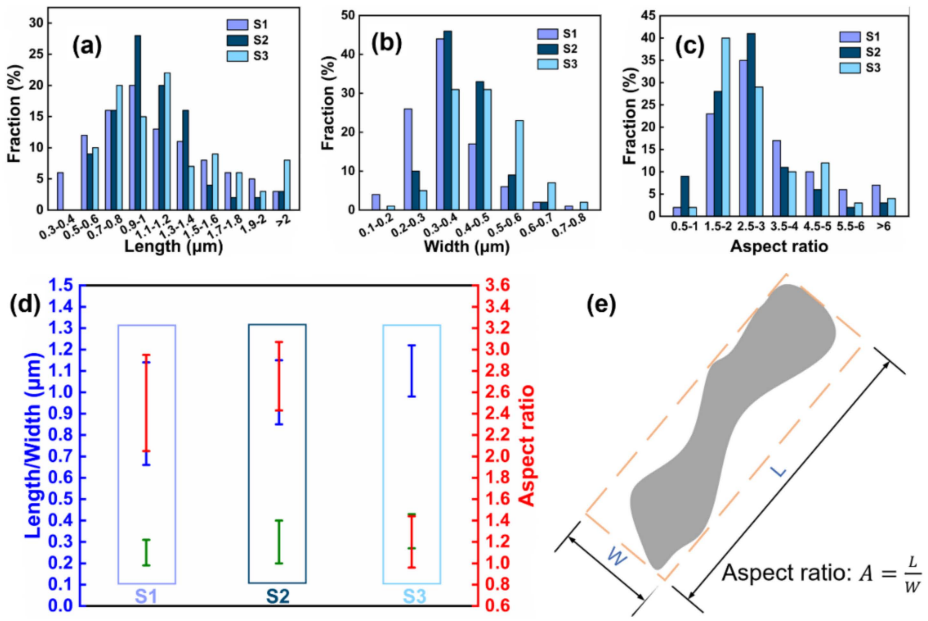

Figure 9. The statistical findings regarding Laves phases in the varied VED samples. (**a**) L (Length), (**b**) W (width), (**c**) aspect ratio, (**d**) the average length, width and aspect ratio of Laves phases, (**e**) the schematic parameter diagram of Laves phase.

The gradual dissolution of the Laves phase consists of three main stages: Laves phase decomposition, solute atom transfer to the γ matrix through boundary and solute atom diffusion [33]. At the beginning of the Laves phase dissolution, three-dimensional diffusion predominantly controlled the process. During the later stage of the dissolution of the Laves phase, the interfacial reaction prevails due to the chemical potential gradient at the interface and the decrease in concentration difference between the Laves phase and the γ matrix, as specified in reference [34]. The δ phase was mainly nucleated at the early stage of heat treatment, so the three-dimensional diffusion mechanism also affected nucleation in the δ phase. The role of Nb in three-dimensional diffusion was significant, and its distribution and diffusion had a considerable impact on the size, morphology and distribution of the δ phase. However, heat treatment of the solution at 980 °C was insufficient to achieve the complete diffusion of Nb. Atoms close to the dissolved Laves phase form diffusion migration first. Therefore, δ phases preferentially produce critical nuclei around the Laves phase [35]. The presence of the Laves phase in the solid solution affected the size and distribution of δ phase in heat treated samples. The contents of Laves phase and δ phase increased with the increase in VED.

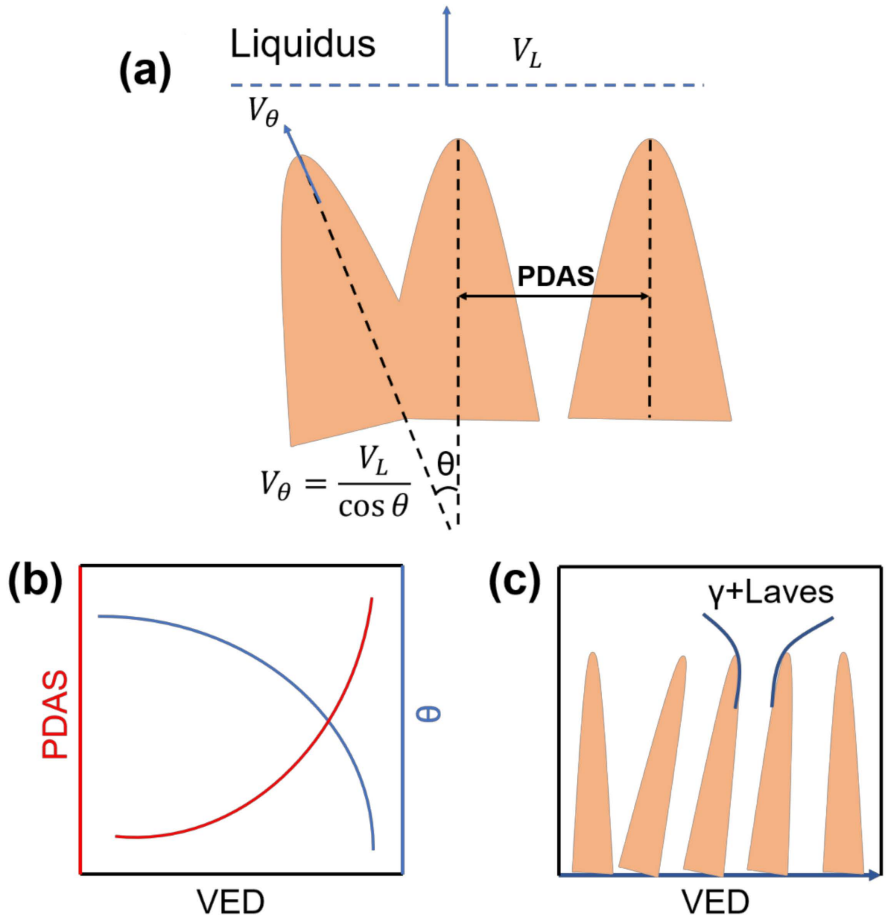

Figure 10. Solidification of columnar dendrites under different VEDs: (**a**) schematic diagram of the competitive grain growth model; (**b**) the relationship between VED and PDAS and misalignment angle θ; (**c**) schematic of solute redistribution under different VED.

3.4. The Influence of Precipitates on Stress Rupture Properties

The longitudinal sections in the rupture fractures were characterized to explain the fracture mechanism, as shown in Figure 11a–c. The plastic deformation ability and stress rupture life of the sample can be indicated by the distribution and length of cracks. The crack length was noticeably shorter in H-S1 than in H-S2 and H-S3. Although the crack distribution in H-S3 was similar to H-S2, the length of cracks was shorter in H-S3 than in H-S2. The cracks primarily occurred at grain boundaries or at the triple point of grain boundaries. The crack number density at approximately 3 mm from the fracture surface of the three sample groups was depicted in Figure 11d. Initially, the samples exhibited a decrease in their crack density as the VED increased. It was found that the crack density is inversely proportional to the durability and elongation of the samples in line with the results of the stress rupture test presented above.

In general, we thought that the long strip of black cracking defects connected together, as shown in Figure 11, and were called micro cracks. Its span size was generally in the range of 1–2 μm. In the creep process, the circular defects that were not connected with the other crack defects were called creep voids. Their sizes were mostly less than 1 μm. Some creep voids would grow up due to tensile stress, as shown in Figure 12b.

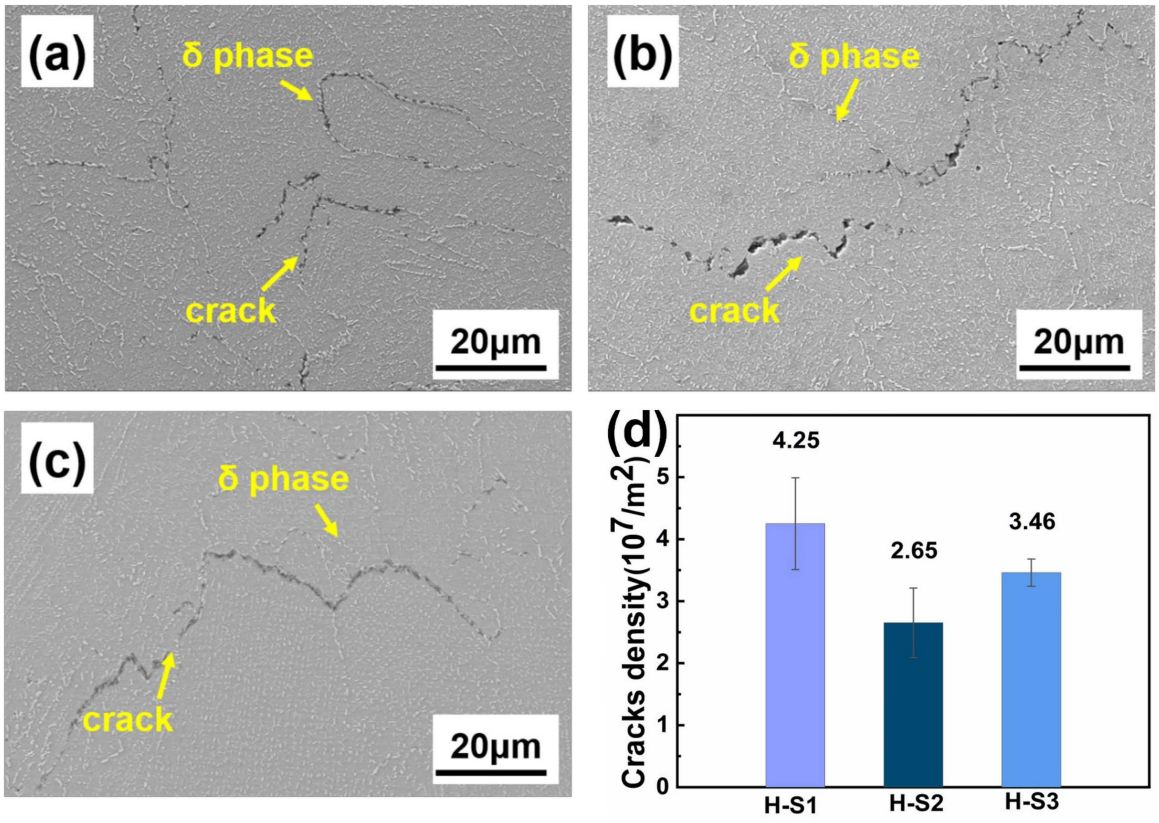

Figure 11. The longitudinal sections of the rupture fractures: (**a**) H-S1, (**b**) H-S2, (**c**) H-S3, (**d**) crack densities of three samples.

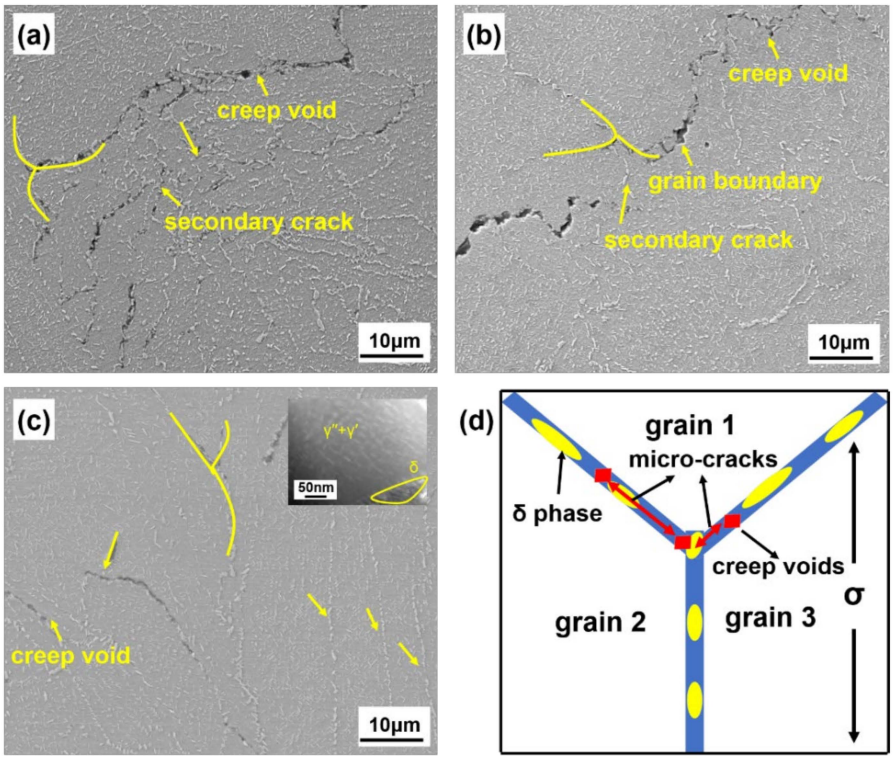

Figure 12. The LPBF IN718 sample after creep: (**a**) H-S1, (**b**) H-S2, and (**c**) H-S3, (**d**) sketch of the creep void and micro-crack formation during creep.

The samples with different VED had an δ phase with different morphologies and sizes after heat treatment. The stress rupture properties were significantly affected by the volume fraction, distribution, and morphologies of the δ phase. As can be seen from Figure 12, the influence of δ-relative durability can be divided into three situations: (1) the δ phase acted as the source of the crack, (2) the crack propagated along the accumulated δ phase, (3) the δ phase affected the precipitation in the γ″ phase, causing cracks. In this investigation, the ratio of the creep temperature (T) to the melting point (T_m) of the IN718 alloy was roughly 0.5. Creep voids had the ability to form and develop at grain boundaries when the T/Tm ratio ranged from 0.3 to 0.6 [19]. Creep voids were found surrounding the δ phase, which was distributed along the grain boundaries, as illustrated in Figure 12a–c. The growth, connection and coalescence of these creep voids resulted in the development of microcracks along the grain boundaries. Furthermore, crack extension could occur at the junction of different grain boundaries due to a disordered atomic arrangement, as shown in Figure 12d.

The S1 had the smallest grain size, and due to the fine-grained material's large grain boundary area per unit volume, there was potential for the nucleation and growth of creep voids at the grain boundaries. The flatter grain boundaries in fine-grained materials made it easier for cracks to propagate. In summary, the H-S1 exhibited the worst stress rupture properties. The uniformly distributed δ phase and suitable grain size in the H-S2 enable it to exhibit optimal stress rupture properties. Groups of δ phases that were aligned parallel to the creep tensile axis were observed in H-S3. These types of δ phases showed minimal impact on the stress rupture properties. However, the δ phase consumed a large amount of the Nb element, so that the γ″ phase could not be sufficiently precipitated in H-S3. Therefore, cracks tended to initiate around a large number of δ phases in the region.

4. Conclusions

In this study, the microstructure evolution and high temperature stress rupture properties of IN718 alloy prepared by LPBF under different VED were analyzed. The following conclusions can be drawn:

1. The existence of the Laves phase in the IN718 alloy was related to the solidification conditions during LPBF process. With an increase in VED, the size and content of Laves phase increased proportionally.
2. After heat treatment, the Laves phase dissolved, resulting in the preferential nucleation of the δ phase in the region where the Laves phase had dissolved in the form of short rods. The volume fraction of δ phase also increased with the increase in VED.
3. Creep voids were easily formed around the δ phase and were distributed along the grain boundary. The inhomogeneous δ phase and fine grains were beneficial to the initiation and propagation of cracks.
4. The δ phase group parallel to the creep tensile axis has little effect on the stress rupture properties. Cracks were more likely to initiate in regions lacking a γ″ phase.

Author Contributions: J.D.: Conceptualization, Investigation, Data curation, Writing—original draft. W.C.: Investigation, Data curation. Y.S.: Conceptualization, Writing—review and editing. R.M.: Investigation, Supervision. H.L.: Funding acquisition, Writing—review and editing, Supervision. X.S.: Resources, Supervision, Project administration. J.Y.: Supervision. C.T.: Writing—review and editing, Supervision, Project administration, Funding acquisition. All authors have read and agreed to the published version of the manuscript.

Funding: The work was supported by the Natural Science Foundation for Excellent Young Scholars of Shangdong Province (ZR2021YQ30) and Zhejiang Key Project of Research and Development Plan (2021C01085) and Key Technology Research Project of Beilun District Ningbo City (2021BLG005).

Data Availability Statement: Data are contained within the article.

Conflicts of Interest: The authors declare no conflict of interest.

References

1. Kim, S.; Choi, H.; Lee, J.; Kim, S. Room and elevated temperature fatigue crack propagation behavior of Inconel 718 alloy fabricated by laser powder bed fusion. *Int. J. Fatigue* **2020**, *140*, 105802. [CrossRef]
2. Pradhan, D.; Mahobia, G.S.; Chattopadhyay, K.; Singh, V. Effect of surface roughness on corrosion behavior of the superalloy IN718 in simulated marine environment. *J. Alloys Compd.* **2018**, *740*, 250–263. [CrossRef]
3. Thakur, D.G.; Ramamoorthy, B.; Vijayaraghavan, L. Study on the machinability characteristics of superalloy Inconel 718 during high speed turning. *Mater. Des.* **2009**, *30*, 1718–1725. [CrossRef]
4. Luo, S.; Huang, W.; Yang, H.; Yang, J.; Wang, Z.; Zeng, X. Microstructural evolution and corrosion behaviors of Inconel 718 alloy produced by selective laser melting following different heat treatments. *Addit. Manuf.* **2019**, *30*, 100875. [CrossRef]
5. Zhao, Z.; Bai, P.; Guan, R.; Murugadoss, V.; Liu, H.; Wang, X.; Guo, Z. Microstructural evolution and mechanical strengthening mechanism of Mg-3Sn-1Mn-1La alloy after heat treatments. *Mater. Sci. Eng. A* **2018**, *734*, 200–209. [CrossRef]
6. Rao, G.A.; Kumar, M.; Srinivas, M.; Sarma, D.S. Effect of standard heat treatment on the microstructure and mechanical properties of hot isostatically pressed superalloy inconel 718. *Mater. Sci. Eng. A* **2003**, *355*, 114–125. [CrossRef]
7. Mantri, S.A.; Dasari, S.; Sharma, A.; Alam, T.; Pantawane, M.V.; Pole, M.; Sharma, S.; Dahotre, N.B.; Banerjee, R.; Banerjee, S. Effect of micro-segregation of alloying elements on the precipitation behaviour in laser surface engineered Alloy 718. *Acta Mater.* **2021**, *210*, 116844. [CrossRef]
8. Zhou, L.; Mehta, A.; McWilliams, B.; Cho, K.; Sohn, Y. Microstructure, precipitates and mechanical properties of powder bed fused inconel 718 before and after heat treatment. *J. Mater. Sci. Technol.* **2019**, *35*, 1153–1164. [CrossRef]
9. Wang, X.; Chou, K. Effects of thermal cycles on the microstructure evolution of Inconel 718 during selective laser melting process. *Addit. Manuf.* **2017**, *18*, 1–14. [CrossRef]
10. Harrison, N.J.; Todd, I.; Mumtaz, K. Reduction of micro-cracking in nickel superalloys processed by Selective Laser Melting: A fundamental alloy design approach. *Acta Mater.* **2015**, *94*, 59–68. [CrossRef]
11. Tucho, W.M.; Cuvillier, P.; Sjolyst-Kverneland, A.; Hansen, V. Microstructure and hardness studies of Inconel 718 manufactured by selective laser melting before and after solution heat treatment. *Mater. Sci. Eng. A* **2017**, *689*, 220–232. [CrossRef]
12. Zhang, S.; Lin, X.; Wang, L.; Yu, X.; Hu, Y.; Yang, H.; Lei, L.; Huang, W. Strengthening mechanisms in selective laser-melted Inconel718 superalloy. *Mater. Sci. Eng. A* **2021**, *812*, 141145. [CrossRef]
13. Watring, D.S.; Benzing, J.T.; Hrabe, N.; Spear, A.D. Effects of laser-energy density and build orientation on the structure–property relationships in as-built Inconel 718 manufactured by laser powder bed fusion. *Addit. Manuf.* **2020**, *36*, 101425. [CrossRef]
14. Liu, S.Y.; Li, H.Q.; Qin, C.X.; Zong, R.; Fang, X.Y. The effect of energy density on texture and mechanical anisotropy in selective laser melted Inconel 718. *Mater. Des.* **2020**, *191*, 108642. [CrossRef]
15. Balbaa, M.; Mekhiel, S.; Elbestawi, M.; McIsaac, J. On selective laser melting of Inconel 718: Densification, surface roughness, and residual stresses. *Mater. Des.* **2020**, *193*, 108818. [CrossRef]
16. Yang, H.; Meng, L.; Luo, S.; Wang, Z. Microstructural evolution and mechanical performances of selective laser melting Inconel 718 from low to high laser power. *J. Alloys Compd.* **2020**, *828*, 154473. [CrossRef]
17. Du, D.; Dong, A.; Shu, D.; Zhu, G.; Sun, B.; Li, X.; Lavernia, E. Influence of build orientation on microstructure, mechanical and corrosion behavior of Inconel 718 processed by selective laser melting. *Mater. Sci. Eng. A* **2019**, *760*, 469–480. [CrossRef]
18. Teng, Q.; Li, S.; Wei, Q.; Shi, Y. Investigation on the influence of heat treatment on Inconel 718 fabricated by selective laser melting: Microstructure and high temperature tensile property. *J. Manuf. Process.* **2021**, *61*, 35–45. [CrossRef]
19. Xu, Z.; Cao, L.; Zhu, Q.; Guo, C.; Li, X.; Hu, X.; Yu, Z. Creep property of Inconel 718 superalloy produced by selective laser melting compared to forging. *Mater. Sci. Eng. A* **2020**, *794*, 139947. [CrossRef]
20. Gao, Y.; Zhang, D.; Cao, M.; Chen, R.; Feng, Z.; Poprawe, R.; Schleifenbaum, J.H.; Ziegler, S. Effect of δ phase on high temperature mechanical performances of Inconel 718 fabricated with SLM process. *Mater. Sci. Eng. A* **2019**, *767*, 138327. [CrossRef]
21. Zhang, S.; Wang, L.; Lin, X.; Yang, H.; Li, M.; Lei, L.; Huang, W. Precipitation behavior of δ phase and its effect on stress rupture properties of selective laser-melted Inconel 718 superalloy. *Compos. Part B Eng.* **2021**, *224*, 109202. [CrossRef]
22. Shi, J.J.; Li, X.; Zhang, Z.X.; Cao, G.H.; Russell, A.M.; Zhou, Z.J.; Li, C.P.; Chen, G.F. Study on the microstructure and creep behavior of Inconel 718 superalloy fabricated by selective laser melting. *Mater. Sci. Eng. A* **2019**, *765*, 138282. [CrossRef]
23. Zhang, D.; Niu, W.; Cao, X.; Liu, Z. Effect of standard heat treatment on the microstructure and mechanical properties of selective laser melting manufactured Inconel 718 superalloy. *Mater. Sci. Eng. A* **2015**, *644*, 32–40. [CrossRef]
24. *E139-11*; Standard Test Methods for Conducting Creep, Creep-Rupture, and Stress-Rupture Tests of Metallic Materials. ASTM International Publish: West Conshohocken, PA, USA, 2018.
25. Bean, G.E.; Witkin, D.B.; McLouth, T.D.; Patel, D.N.; Zaldivar, R.J. Effect of laser focus shift on surface quality and density of Inconel 718 parts produced via selective laser melting. *Addit. Manuf.* **2018**, *22*, 207–215. [CrossRef]
26. Song, K.; Yu, K.; Lin, X.; Chen, J.; Yang, H.; Huang, W. Microstructure and mechanical properties of heat treatment laser solid forming superalloy Inconel 718. *Jinshu Xuebao/Acta Metall. Sin.* **2015**, *51*, 935–942. [CrossRef]
27. Kumara, C.; Balachandramurthi, A.R.; Goel, S.; Hanning, F.; Moverare, J. Toward a better understanding of phase transformations in additive manufacturing of Alloy 718. *Materialia* **2020**, *13*, 100862. [CrossRef]
28. Zhou, K.; Wang, Z.; He, F.; Liu, S.; Li, J.; Kai, J.-j.; Wang, J. A precipitation-strengthened high-entropy alloy for additive manufacturing. *Addit. Manuf.* **2020**, *35*, 101410. [CrossRef]

29. Li, J.; Zhao, Z.; Bai, P.; Qu, H.; Liu, B.; Li, L.; Wu, L.; Guan, R.; Liu, H.; Guo, Z. Microstructural evolution and mechanical properties of IN718 alloy fabricated by selective laser melting following different heat treatments. *J. Alloys Compd.* **2019**, *772*, 861–870. [CrossRef]
30. Sui, S.; Tan, H.; Chen, J.; Zhong, C.; Li, Z.; Fan, W.; Gasser, A.; Huang, W. The influence of Laves phases on the room temperature tensile properties of Inconel 718 fabricated by powder feeding laser additive manufacturing. *Acta Mater.* **2019**, *164*, 413–427. [CrossRef]
31. Paul, S.; Liu, J.; Strayer, S.T.; Zhao, Y.; Sridar, S.; Klecka, M.A.; Xiong, W.; To, A.C. A Discrete Dendrite Dynamics Model for Epitaxial Columnar Grain Growth in Metal Additive Manufacturing with Application to Inconel. *Addit. Manuf.* **2020**, *36*, 101611. [CrossRef]
32. Yuan, C.; Lu, F.; Zhang, K.; Nie, P.; Hosseini, R.; Feng, K.; Li, Z. Dendritic microstructure and hot cracking of laser additive manufactured Inconel 718 under improved base cooling. *J. Alloys Compd.* **2016**, *670*, 312–321. [CrossRef]
33. Zhang, S.; Wang, L.; Lin, X.; Yang, H.; Huang, W. The formation and dissolution mechanisms of Laves phase in Inconel 718 fabricated by selective laser melting compared to directed energy deposition and cast. *Compos. Part B Eng.* **2022**, *239*, 109994. [CrossRef]
34. Zhang, S.; Lin, X.; Wang, L.; Yu, X.; Yang, H.; Lei, L.; Huang, W. Influence of grain inhomogeneity and precipitates on the stress rupture properties of Inconel 718 superalloy fabricated by selective laser melting. *Mater. Sci. Eng. A* **2021**, *803*, 140702. [CrossRef]
35. Cao, G.H.; Sun, T.Y.; Wang, C.H.; Li, X.; Liu, M.; Zhang, Z.X.; Hu, P.F.; Russell, A.M.; Schneider, R.; Gerthsen, D.; et al. Investigations of γ', γ'' and δ precipitates in heat-treated Inconel 718 alloy fabricated by selective laser melting. *Mater. Charact.* **2018**, *136*, 398–406. [CrossRef]